INTERNATIONAL JOURNAL FOR NUMERICAL METHODS IN FLUIDS
Int. J. Numer. Meth. Fluids 2005; **49**:75–98
Published online 8 June 2005 in Wiley InterScience (www.interscience.wiley.com). DOI: 10.1002/fld.995

Assessment of non-Fickian subgrid-scale models for passive scalar in a channel flow

E. Montreuil[1,*,†], O. Labbé[1,‡] and P. Sagaut[2,§]

[1] *Office National d'Études et de Recherches Aérospatiales, BP72, 29 Av. de la Division Leclerc, F-92322 Châtillon Cedex, France*
[2] *Université Pierre et Marie Curie, boîte 162, 4 Place Jussieu, F-75252 Paris Cedex 05, France*

SUMMARY

In order to assess new subgrid-scale (SGS) models for a passive scalar, several large eddy simulations of a turbulent channel flow with passive scalar, for various Prandtl numbers ranging from 0.1 to 2.0 are carried out. These models are not based on the classical Fickian approximation and do not necessarily induce an alignment between the SGS heat flux vector and the gradient of the resolved temperature. Five SGS models are investigated on two grids. To validate the simulations, statistical quantities such as mean temperature, temperature variance and turbulent heat flux are compared with available data obtained by direct numerical simulation (DNS). The SGS dissipation is computed for different models in order to analyse its behaviour. The turbulence structures based on instantaneous velocity and temperature are described to study the correlations between these two fields. Among the assessed models, those consisting in Fickian and non-Fickian parts seem to be full of promise. Copyright © 2005 John Wiley & Sons, Ltd.

KEY WORDS: large eddy simulation (LES); passive scalar; turbulent channel flow; subgrid-scale (SGS) model

1. INTRODUCTION

Understanding and prediction of heat transfer are of great importance in the engineering domain. Heat transfer problems in heat exchangers, gas turbines and nuclear reactors or pollution dispersal are few examples. For small temperature differences, the temperature acts like a passive scalar driven by the turbulent velocity field without influencing the latter. In this case,

*Correspondence to: Emmanuel Montreuil, Office National d'Études et de Recherches Aérospatiales, BP72, 29 Av. de la Division Leclerc, F-92322 Châtillon Cedex, France.
†E-mail: emmanuel.montreuil@onera.fr
‡E-mail: odile.labbe@onera.fr
§E-mail: sagaut@lmm.jussieu.fr

Received 21 December 2004
Revised 18 April 2005
Accepted 23 April 2005

the temperature field is determined by solving a temperature conservation equation for a given turbulent velocity.

The flow between two parallel unbounded plates has been already studied experimentally or numerically [1–5]. In return, few direct simulations or large eddy simulations are at our disposal, if we consider the turbulent transfer of a passive scalar (or temperature field) in a channel. The first direct simulation for the passive scalar transport is due to Kim and Moin [6]. The studied flow corresponds to a fluid, containing an internal heat source, which exhausts through cold walls of the channel. This simulation confirmed the high correlation between streamwise velocity and temperature fluctuations, which has been experimentally observed [7]. Lyons [8, 9] presented similar results in the case of turbulent transport of temperature field. In his case, both walls conditions are isothermal, but the bottom wall temperature is hot, while the top one is maintained at a cold temperature. Kasagi *et al.* [10, 11] have carried out the same kind of direct simulation of passive scalar, but the thermal conditions are different: they used an isoflux condition for both walls. Some authors such as Calmet *et al.* [12] and Dong *et al.* [13] used large eddy simulation to study polluent transport, represented by its concentration, which corresponds to high Schmidt numbers. Moreover, Kawamura *et al.* [14, 15] continued Kasagi's works in studying the turbulent transport of temperature field for Prandtl numbers varying from 0.025 to 5. At last, Wang *et al.* [16] carried out turbulent oscillatory heat transfer in channel flows.

Large eddy simulation (LES) involves the parametrization of high frequencies of the solution through the use of a subgrid-scale (SGS) model [17]. Among various levels of models, Fickian models, i.e. those of eddy diffusivity as well as eddy viscosity, are most used mainly thanks to their simplicity. In almost all eddy-diffusivity models, the SGS scalar flux is parametrized using the concept of isotropic eddy diffusivity. A drawback of such models is that they cannot predict the anisotropy of SGS scalar flux that arises from the resolved velocity gradient, which is associated with coherent structures in the near-wall region. It has been known for a long time that the turbulent diffusivity in turbulent shear flows has different values for different orientations of the mean scalar gradient, yielding a non-diagonal SGS-diffusivity tensor. Some authors have also given arguments against the self-consistency of gradient transport models with spatially varying turbulent diffusivities [18].

Previously, the authors [5] have compared several SGS Reynolds tensor models without passive scalar model, for two friction Reynolds numbers (180 and 400). In order to study SGS scalar flux models and to avoid discrepancies from the aerodynamical flow, the authors have chosen a rather low-friction Reynolds number (180) in an academic geometry. Otherwise, a more complex geometry (a backward-facing step) has been simulated by Labbé *et al.* [19] in which the heat transfer phenomenon in the reattachment zone was investigated with the mixed scale subgrid model.

In this work, we will present results obtained with Fickian and non-Fickian SGS models for scalar flux in the plane channel configuration at a friction Reynolds number equal to 180, for three Prandtl values (0.1, 0.71 and 2.0). Governing equations and the numerical method are presented in Section 2. The SGS model used in the momentum equation is described in Section 3. Details of the selected SGS models for the scalar flux are given in Section 4. Section 5 is devoted to the statistical results with the Prandtl effect. Section 6 presents instantaneous velocity and temperature fields, showing phenomena such as sweeps and ejections. Conclusions are given in Section 7.

2. GOVERNING EQUATIONS AND NUMERICAL METHOD

2.1. Mathematical model

The fluid is supposed to be incompressible with no buoyancy effect: the temperature field is considered as a passive scalar. Therefore, the retained variables for the simulation are the resolved velocity field $\overline{u}$ and the resolved temperature increment $\overline{\Theta}$, which is defined as

$$\overline{\Theta}(x,y,z;t)=\frac{\overline{T}(x,y,z;t)-T_l(x)}{T_0} \tag{1}$$

where T_l and T_0 are, respectively, the temperature associated with static streamwise varying solution and the reference temperature [10]. The resulting dimensionless governing equations read

$$\frac{\partial \overline{u}_i}{\partial x_i}=0 \tag{2}$$

$$\frac{\partial \overline{u}_i}{\partial t}+\frac{\partial}{\partial x_j}(\overline{u}_j\overline{u}_i)=-\frac{\partial \overline{\Pi}}{\partial x_i}+\frac{1}{Re}\frac{\partial^2 \overline{u}_i}{\partial x_j \partial x_j}-\frac{\partial \tau_{ij}^d}{\partial x_j}+F_0(t)\delta_{i1} \tag{3}$$

$$\frac{\partial \overline{\Theta}}{\partial t}+\frac{\partial}{\partial x_j}(\overline{\Theta}\,\overline{u}_j)=\frac{1}{PrRe}\frac{\partial^2 \overline{\Theta}}{\partial x_j \partial x_j}-\frac{\partial \tau_{\theta j}}{\partial x_j}+\dot{Q} \tag{4}$$

with $\tau_{ij}=\overline{u_iu_j}-\overline{u}_i\overline{u}_j$, $\tau_{ij}^d=\tau_{ij}-\frac{1}{3}\tau_{kk}$, $\tau_{\theta j}=\overline{\Theta u_j}-\overline{\Theta}\overline{u}_j$. The pseudo-pressure $\overline{\Pi}=\overline{P}+\tau_{kk}/3$ is computed by solving the associated Poisson equation [20]. The term $F_0(t)$ is related to the time-adaptive forcing term which is used to enforce a constant mass flowrate across the channel [5]. The source/sink $\dot{Q}$ guarantees the bulk temperature conservation [10]. It is important to notice that this source/sink term is related to the choice of an isoflux condition that will be detailed in the next section. In any case, it does not correspond to an unphysical source/sink term added to ensure bulk temperature conservation. It is defined by the following dimensionless relationship:

$$\dot{Q}=-\frac{\mathrm{d}T_l}{\mathrm{d}x}\,\overline{u}_1=-\frac{q_\mathrm{w}}{u_\mathrm{b}}\,\overline{u}_1 \tag{5}$$

where u_b and q_w are, respectively, the bulk velocity and the mean heat flux at the wall which are defined by

$$u_\mathrm{b}=\frac{1}{2h}\int_0^{2h}\overline{u}_1\,\mathrm{d}z \qquad u_\mathrm{w}=\sqrt{\left|\nu\frac{\partial \overline{u}_1}{\partial z}\right|_{z=0}} \qquad q_\mathrm{w}=\frac{\kappa\left.\dfrac{\partial \overline{\Theta}}{\partial z}\right|_{z=0}}{u_\mathrm{w}} \tag{6}$$

2.2. Boundary and initial conditions

For the resolved velocity field, periodic conditions are used in streamwise and spanwise directions, while no-slip condition is applied on the two solid walls.

An isoflux condition [15] on solid walls and periodic conditions in the other directions (as for the velocity field) are used for the resolved temperature field. The isoflux condition means that the time-averaged wall heat flux does not change in the streamwise direction. This heating condition is equivalent to an assumption that the wall ensemble-averaged temperature over the spanwise direction and time should increase linearly in the streamwise direction. The isoflux condition requires to impose zero-boundary condition for the resolved temperature field on the two walls, i.e. $\overline{\Theta}_{\text{wall}} = 0$.

The initial resolved velocity field is obtained through the superposition between a Poiseuille profile and a free divergence perturbation. The resolved temperature field is initialized by an instantaneous streamwise velocity component issued by previous calculations [5], yielding $\overline{\Theta}(t=0) = Pr\overline{u}_1$.

2.3. Numerical method

The time integration is performed using a second-order accurate semi-implicit method. Convection terms are written in skew-symmetric form and treated by using an explicit second-order Adams–Bashforth scheme. The molecular diffusion terms are discretized using the implicit second-order backward differentiation formulae (BDF). The spatial discretization is achieved using a second-order hybrid Finite Element/Finite Difference approach. A full description of the method can be found in Reference [5].

3. SGS MODELLING IN MOMENTUM EQUATION

In order to isolate the differences due to the treatment of the SGS scalar flux, the same SGS model was used in the momentum equation for all the computations. The selected model is an eddy-viscosity model, called the selective mixed scale model (MSM). This model was shown to lead to a good overall agreement with direct numerical simulation (DNS) data for this configuration, on the same mesh and using the same numerical method [5]. The deviatoric part of the SGS tensor τ_{ij}^d appearing in the momentum equation (3) is assumed to be proportional to the resolved strain rate tensor:

$$\tau_{ij}^d = -2\nu_{sm}\overline{S}_{ij}, \quad \nu_{sm} = C_m f_{\text{selec}} \overline{\Delta}^{3/2} \|\overline{\nabla} \wedge \overline{u}\|^{1/2} \sqrt{q_c} \tag{7}$$

where $\overline{S}_{ij} = \frac{1}{2}((\partial\overline{u}_i/\partial x_j) + (\partial\overline{u}_j/\partial x_i))$, $\|\overline{\nabla} \wedge \overline{\mathbf{u}}\|$ is the norm of the curl vector, the cut-off length-scale $\overline{\Delta}$ is defined as $(\Delta x \Delta y \Delta z)^{1/3}$, q_c is the kinetic energy of the highest resolved frequencies, and f_{selec} a selection function (see References [17, 21] for a full description of the model). The constant C_m of the model is set to 0.1, which corresponds to its theoretical value for isotropic turbulence. The kinetic energy q_c is evaluated by applying a test filter to the resolved field:

$$q_c = \tfrac{1}{2}(\overline{u}_i - \widetilde{\overline{u}}_i)^2 \tag{8}$$

4. SGS MODELLING IN TEMPERATURE EQUATION

We now present the selected models for the SGS scalar flux. All of them can be recast in the following general form:

$$\tau_{\theta j} = f(\overline{u}, \overline{\Theta}, \overline{\Delta}) \frac{\partial \overline{\Theta}}{\partial x_j} + g(\overline{u}, \overline{\Theta}, \overline{\Delta}) V_j \tag{9}$$

where f and g are two scalar functions and V a vector which is not necessarily aligned with the resolved temperature gradient.

The first part of Equation (9) corresponds to the Fickian part of the model, and the function of proportionality f is termed an SGS diffusivity, by analogy with the molecular diffusivity.

The second part of the model, which is associated with the function g and vector V is introduced to break the alignment of the SGS flux vector and the resolved field gradient. Five models are now described, which correspond to different definitions of the two parts of the SGS scalar flux.

4.1. Dynamic linear combination models

The two first models belong to the class of the dynamic linear combination models, as defined by Salvetti and Banerjee [22]. The non-Fickian part of the model is evaluated using a scale-similarity model, leading to

$$\tau_{\theta j} = -C_\kappa \overline{\Delta}^2 |\overline{S}| \frac{\partial \overline{\Theta}}{\partial x_j} + C'_\kappa (\overline{\overline{u}_j \overline{\Theta}} - \overline{\overline{u}}_j \overline{\overline{\Theta}}) \tag{10}$$

where $|\overline{S}| = \sqrt{2\overline{S}_{ij}\overline{S}_{ij}}$. The two variables $C_\kappa = C_\kappa(z;t)$ and $C'_\kappa = C'_\kappa(z;t)$ of the model are evaluated by using a dynamic procedure, or can be taken equal to a given theoretical value. To compute dynamically these two constants, it is necessary to introduce a test filter whose filter width $\widetilde{\overline{\Delta}}$ is larger than the grid filter width $\overline{\Delta}$.

Following the Germano–Lilly procedure [23], the closure for the scalar flux at the test-filter level can be written as

$$T_{\theta j} = -C_\kappa \widetilde{\overline{\Delta}}^2 |\widetilde{\overline{S}}| \frac{\partial \widetilde{\overline{\Theta}}}{\partial x_j} + C'_\kappa (\widetilde{\overline{u}_j \overline{\Theta}} - \widetilde{\overline{u}}_j \widetilde{\overline{\Theta}}) \tag{11}$$

The Germano identity for the scalar flux reads

$$F_j = -C_\kappa H_j + C'_\kappa G_j \tag{12}$$

where the vectors F_j, H_j and G_j are defined by

$$F_j = \widetilde{\overline{u}_j \overline{\Theta}} - \widetilde{\overline{u}}_j \widetilde{\overline{\Theta}} \equiv T_{\theta j} - \widetilde{\tau}_{\theta j} \tag{13}$$

$$H_j = \widetilde{\overline{\Delta}^2 |\widetilde{\overline{S}}|} \frac{\partial \widetilde{\overline{\Theta}}}{\partial x_j} - \overline{\Delta}^2 \widetilde{|\overline{S}| \frac{\partial \overline{\Theta}}{\partial x_j}} \tag{14}$$

$$G_j = \widetilde{\overline{\overline{u}_j} \overline{\overline{\Theta}}} - \widetilde{\overline{u}_j} \widetilde{\overline{\overline{\Theta}}} \tag{15}$$

4.1.1. Case HSDBD. The first model, referred to as HSDBD, corresponds to the case where the two constants are evaluated through the dynamic procedure. They are computed by solving the following linear system, which is obtained by contracting Equation (12) with the vectors H_j and G_j:

$$\begin{aligned} -C_\kappa (H_j H_j) + C'_\kappa (G_j H_j) &= (F_j H_j) \\ -C_\kappa (H_j G_j) + C'_\kappa (G_j G_j) &= (F_j G_j) \end{aligned} \tag{16}$$

4.1.2. Case HSDB. For this model, referred to as HSDB, the constant C'_κ is set to 1, as usually done for non-dynamic scale-similarity models. Therefore, the constant C_κ is evaluated by only contracting (12) with the vector H_j:

$$-C_\kappa (H_j H_j) + (G_j H_j) = (F_j H_j) \tag{17}$$

$$C_\kappa = -\frac{\langle F_j H_j - G_j H_j \rangle}{\langle H_j H_j \rangle} \tag{18}$$

The use of vector H_j for the contraction leads to a stable procedure, which does not require clipping of the constant. The statistical average operator $\langle\,\rangle$ over planes parallel to the wall is introduced to stabilize the dynamic procedure.

4.1.3. Case S_dyn. For this last dynamic model, referred to as S_dyn, the constant C'_κ is set to zero, resulting in a classical dynamic eddy-diffusivity model. The remaining constant C_κ is classically computed as

$$C_\kappa = -\frac{\langle F_j H_j \rangle}{\langle H_j H_j \rangle} \tag{19}$$

4.2. Explicit vectorial model (EVM)

Here, we propose a new non-Fickian SGS model for the scalar flux, which is based on the second-order non-linear expansion of the SGS terms. It can be seen as the extension for LES of the RANS closure derived by Yoshizawa [24]. The subgrid scalar flux is written as

$$\begin{aligned} -\tau_{\theta j} &= C_1 \varepsilon'_u \left(\frac{K'_\theta}{\varepsilon'_\theta}\right)^2 \frac{\partial \overline{\Theta}}{\partial x_j} - \varepsilon'_u \left(\frac{K'_\theta}{\varepsilon'_\theta}\right)^3 (C_2 \overline{S}_{jl} + C_3 \overline{\Omega}_{jl}) \frac{\partial \overline{\Theta}}{\partial x_l} \\ C_1 &= 0.446, \quad C_2 = 0.37, \quad C_3 = 0.21 \end{aligned} \tag{20}$$

where $\varepsilon'_u, \varepsilon'_\theta, K'_\theta$ are, respectively, the SGS dissipation rate of kinetic energy, the SGS dissipation of temperature variance and the SGS temperature variance. The tensor $\overline{\Omega}_{ij} = \frac{1}{2}((\partial \overline{u}_i/\partial x_j) - (\partial \overline{u}_j/\partial x_i))$ is related to the skew-symmetric part of the resolved velocity gradient. Under the

local equilibrium hypothesis, the SGS dissipation rate of kinetic energy and the SGS dissipation of temperature variance can be evaluated as [25]:

$$\varepsilon'_u = 0.845\,\frac{q_c^{3/2}}{\overline{\Delta}}, \quad \varepsilon'_\theta = 2.02\,\frac{q_c^{1/2}K'_\theta}{\overline{\Delta}} \tag{21}$$

while the SGS temperature variance is evaluated using a scale-similarity hypothesis:

$$K'_\theta = \overline{\theta}'\overline{\theta}' \simeq (\overline{\theta} - \widetilde{\overline{\theta}})^2 \tag{22}$$

4.3. Constant SGS Prandtl model

In order to emphasize the effect of non-Fickian SGS models, a classical SGS-diffusivity model, referred to as MSM, with a constant SGS Prandtl number taken equal to 0.6, has also been considered (value recommended by the authors in References [26–28]).

5. STATISTICAL RESULTS

All the five SGS models proposed for the scalar flux have been implemented and used to simulate the case of a heated plane channel flow. Table I summarizes the Fickian and non-Fickian parts of the models.

The friction Reynolds number Re_τ and Prandtl number are, respectively, 180 and 0.71, corresponding to the DNS data of Kawamura *et al.* [15]. The associated value of the bulk Reynolds number Re_b is 5500. The computational domain size is chosen to be, respectively, $4\pi h$ and πh in the streamwise (x) and spanwise (y) directions, where h is the half channel height. Following Kim *et al.* [2], this domain size is sufficiently large. In order to analyse the effect of the resolution, two computational grids are considered: a fine one with $64 \times 64 \times 67$ grid points ($\Delta x^+ = 35, \Delta y^+ = 9, \Delta z^+_{\min} = 1$), and a coarse one including $32 \times 32 \times 67$ grid points ($\Delta x^+ = 70, \Delta y^+ = 18, \Delta z^+_{\min} = 1$). In order to assess the effect of the SGS models, a case without SGS model for the scalar flux, referred to as DNSc, has also been considered.

Table I. Fickian and non-Fickian parts for the tested subgrid-scale heat flux models.

Cases	Fickian part (f)	non-Fickian part ($g.V_j$)
MSM	$-\dfrac{C_m}{Pr_{sm}}\|\overline{\nabla} \wedge \overline{u}\|^{1/2} q_c^{1/2}\overline{\Delta}^{3/2}.f_{\text{selec}}$	0
HSDBD	$-C_\kappa(z;t)\overline{\Delta}^2\|\overline{S}\|$	$C'_\kappa(z;t)(\overline{\overline{u}_j\overline{\Theta}} - \overline{\overline{u}}_j\overline{\overline{\Theta}})$
HSDB	$-C_\kappa(z;t)\overline{\Delta}^2\|\overline{S}\|$	$(\overline{\overline{u}_j\overline{\Theta}} - \overline{\overline{u}}_j\overline{\overline{\Theta}})$
S_dyn	$-C_\kappa(z;t)\overline{\Delta}^2\|\overline{S}\|$	0
EVM	$-C_1\varepsilon'_u\left(\dfrac{K'_\theta}{\varepsilon'_\theta}\right)^2$	$2\varepsilon'_u\left(\dfrac{K'_\theta}{\varepsilon'_\theta}\right)^3(C_2\overline{S}_{ij} + C_3\overline{\Omega}_j)\dfrac{\partial\overline{\Theta}}{\partial x_j}$
DNSc	0	0

Statistical moments of the solution have been computed by performing an average in time and over plane parallel to the walls. Because the effective filter of the *a posteriori* tests remains unknown, it is impossible to filter the DNS data in a proper way or to defilter the LES data. DNS values can be considered as target values for the first-order moments only.

There are two possible choices for the normalization of the statistical results: wall normalization (velocity and temperature friction) and bulk normalization (bulk velocity and temperature). Our choice of forcing terms guarantees bulk values. So, in order to compare the effect of the models in the simulation, the second choice avoids errors introduced by wall quantities calculations. However, the wall normalization will be used for comparison with empirical laws or DNS data because of the wall values guaranteed by their forcing terms.

5.1. *Temperature field*

The computed mean profiles of the temperature, normalized by the bulk value, are shown in Figures 1 and 2. A satisfactory agreement with reference data is observed on both grids. The resolved scalar variance profiles are shown in Figures 3 and 4. All the models lead to a good prediction of the location of the maximal value of the variance in the buffer layer, but they yield a large overprediction of the absolute value of the peak on the coarse grid. On the fine grid, the variance and streamwise scalar flux (not presented here for briefness) are still overpredicted. This could be induced by the classical overprediction of the streamwise turbulent intensity.

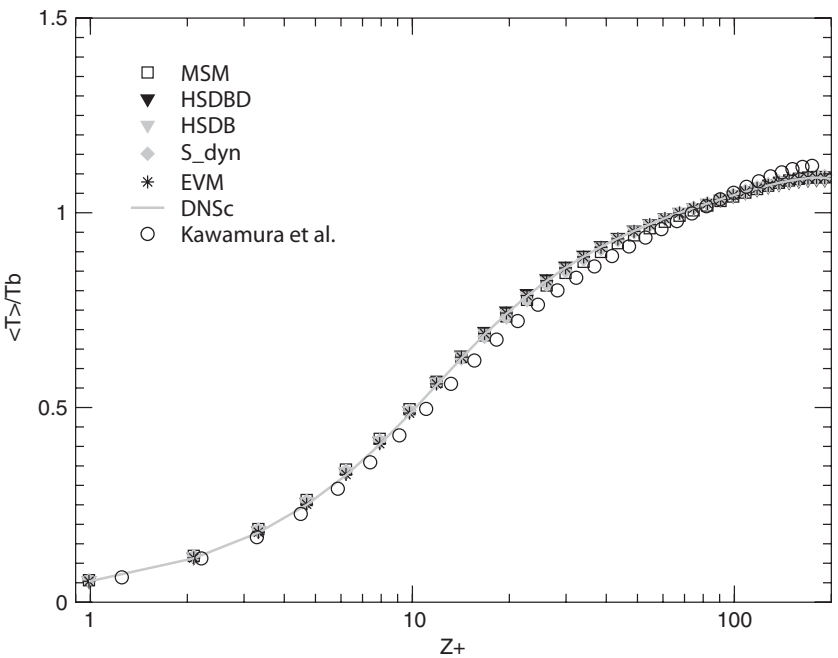

Figure 1. Mean temperature profiles normalized by the bulk temperature: fine grid.

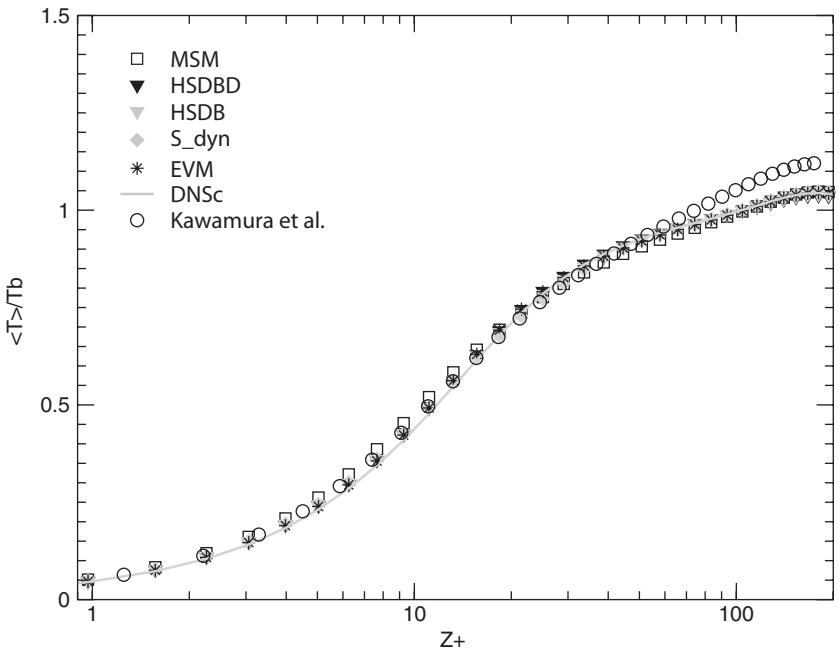

Figure 2. Mean temperature profiles normalized by the bulk temperature: coarse grid.

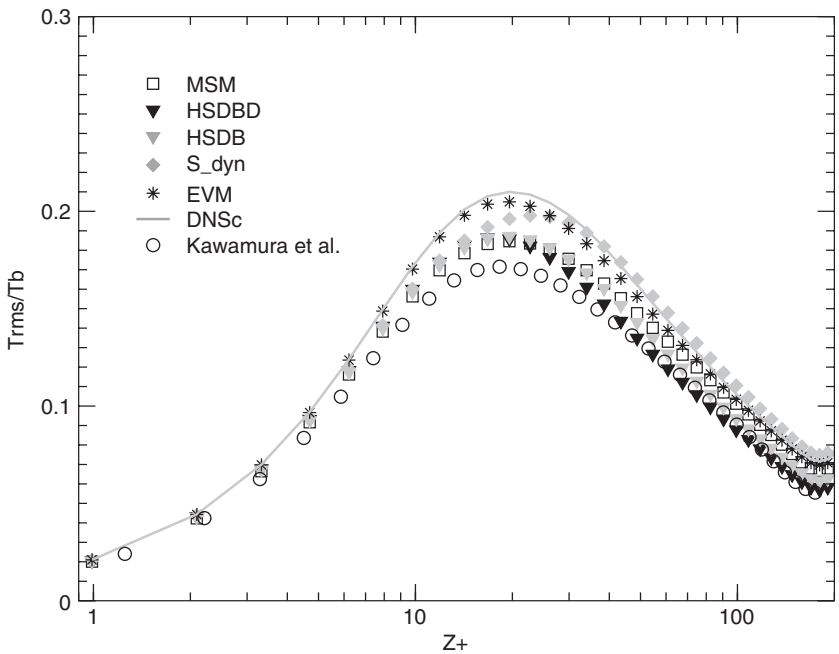

Figure 3. Root mean square temperature profiles normalized by the bulk temperature: fine grid.

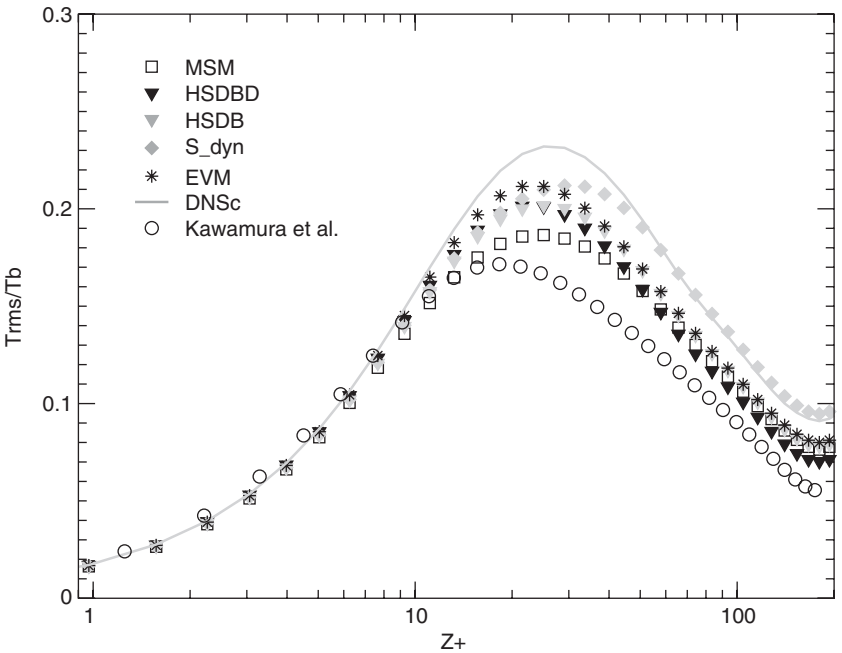

Figure 4. Root mean square temperature profiles normalized by the bulk temperature: coarse grid.

The best overall quality of the results on the fine grid is obtained using the two linear combination models (HSBDB/HSBD). On the coarse grid, results provided by the linear combination models are still among the best ones, although the MSM case is observed to significantly improve the results. This might be explained by the fact that, on the coarse grid, the most desired effect of the SGS models should be a diffusive one.

The resolved turbulent Prandtl number Pr_t^{RES}, defined as

$$Pr_t^{RES} = \frac{\overline{u'w'}(\partial\overline{\Theta}/\partial z)}{\overline{w'\Theta'}(\partial\overline{u}/\partial z)} \tag{23}$$

is shown in Figures 5 and 6. All the SGS models yield the same shape of the profile on both grids, but a better agreement is obtained with DNS data of Kawamura *et al.* [15] on the fine grid. Following DNS data of Kawamura, this quantity is almost constant (around 1) in the viscous and buffer layers ($z^+ < 30$).

5.2. *Analysis of the SGS models*

In order to get a deeper insight into the behaviour of the SGS models, we now provide some results dealing with the SGS dissipation of the scalar variance $\varepsilon_\Theta = -\tau_\Theta \cdot \nabla\overline{\Theta}$. This dissipation can be split as the sum of two contributions:

$$\varepsilon_\Theta = \varepsilon_\Theta^F + \varepsilon_\Theta^{NF} \tag{24}$$

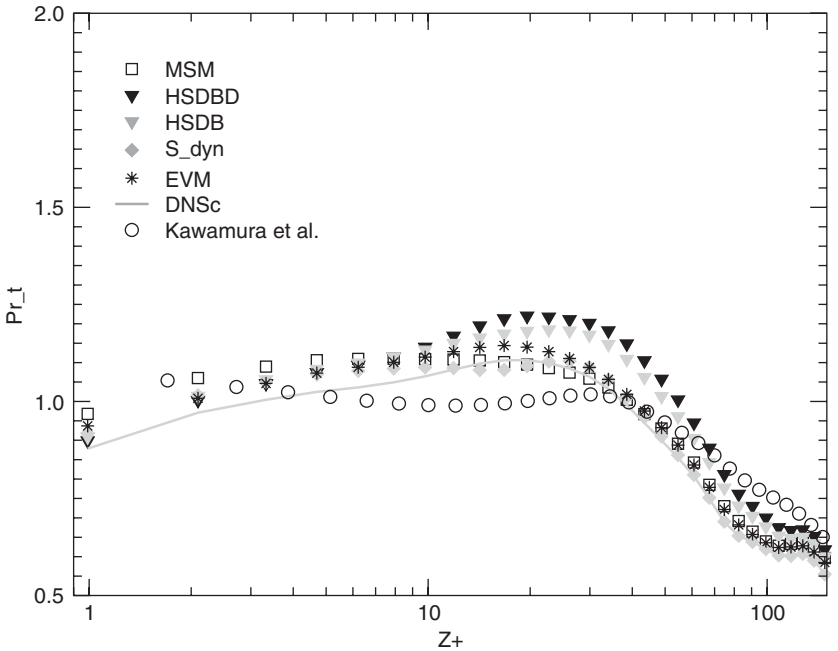

Figure 5. Mean turbulent Prandtl number: fine grid.

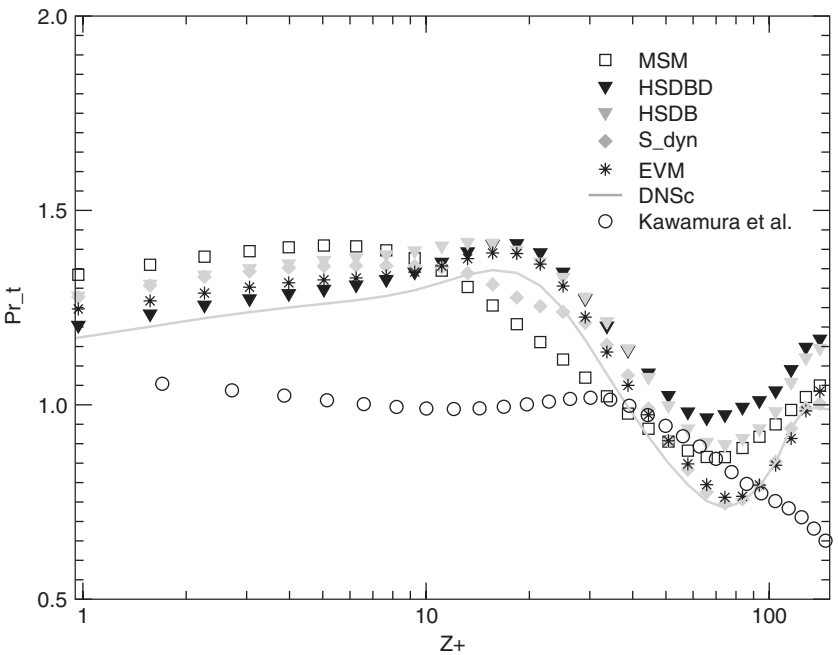

Figure 6. Mean turbulent Prandtl number: coarse grid.

where $\varepsilon_\Theta^{\mathrm{F}}$ and $\varepsilon_\Theta^{\mathrm{NF}}$ are the contributions associated, respectively, with the Fickian and non-Fickian part of the model. Mean value profiles of these two quantities, computed on the fine grid, are displayed in Figures 7 and 8. The non-Fickian parts of the HSDBD and HSDB model yield the same level of dissipation, but a very interesting difference is observed when looking at the contribution of the Fickian part: the HSDB remains positive, while the HSDBD becomes negative, allowing the representation of backscatter phenomena. But, for these two models, the dissipation associated with the non-Fickian part is dominant, resulting in a global positive dissipation. The comparison of the $\varepsilon_\Theta^{\mathrm{F}}$ of the three dynamic models reveals that the linear combination results in a diminution of its importance.

According to Härtel and Kleiser [29], we now consider a second possible splitting of the scalar variance dissipation, as the sum of the dissipation associated with the mean temperature gradient, referred to as $\varepsilon_\Theta^{\mathrm{MS}}$, and the dissipation associated with the fluctuating field, referred to as $\varepsilon_\Theta^{\mathrm{FS}}$, with

$$\varepsilon_\Theta^{\mathrm{MS}} = -\langle \tau_\Theta \rangle \cdot \langle \nabla \overline{\Theta} \rangle, \quad \varepsilon_\Theta^{\mathrm{FS}} = -\langle \tau_\Theta'' \cdot (\nabla \overline{\Theta})'' \rangle \tag{25}$$

where the fluctuating part of a dummy variable ϕ is defined as $\phi'' = \phi - \langle \phi \rangle$, and $\langle\rangle$ denotes the statistical average. Profiles obtained on the fine grid are plotted in Figures 9 and 10. All the models predict that maximal value of the dissipation occurs in the buffer layer ($\varepsilon_\Theta^{\mathrm{MS}}$) or at the beginning of the logarithmic layer ($\varepsilon_\Theta^{\mathrm{FS}}$), in agreement with previous results obtained for the kinetic energy dissipation. An important fact is that the MSM is the only SGS model which predicts the existence of a backscatter zone in the buffer layer: it is seen that the dissipation

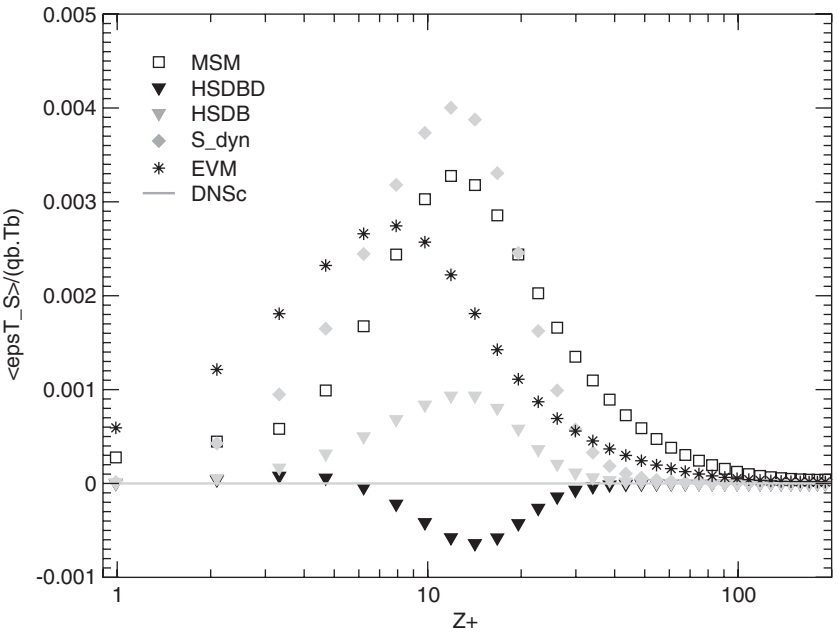

Figure 7. Mean SGS dissipation of the scalar variance (fine grid): Fickian part.

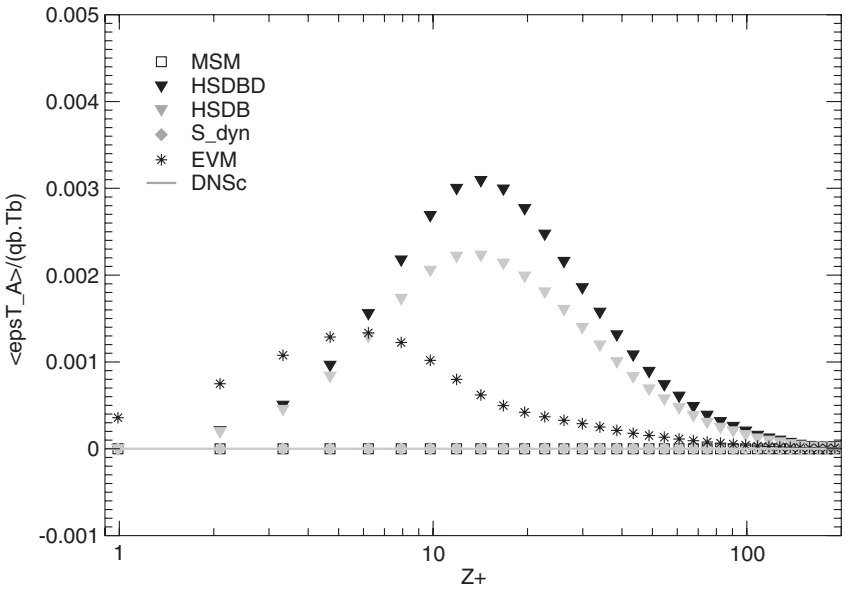

Figure 8. Mean SGS dissipation of the scalar variance (fine grid): non-Fickian part.

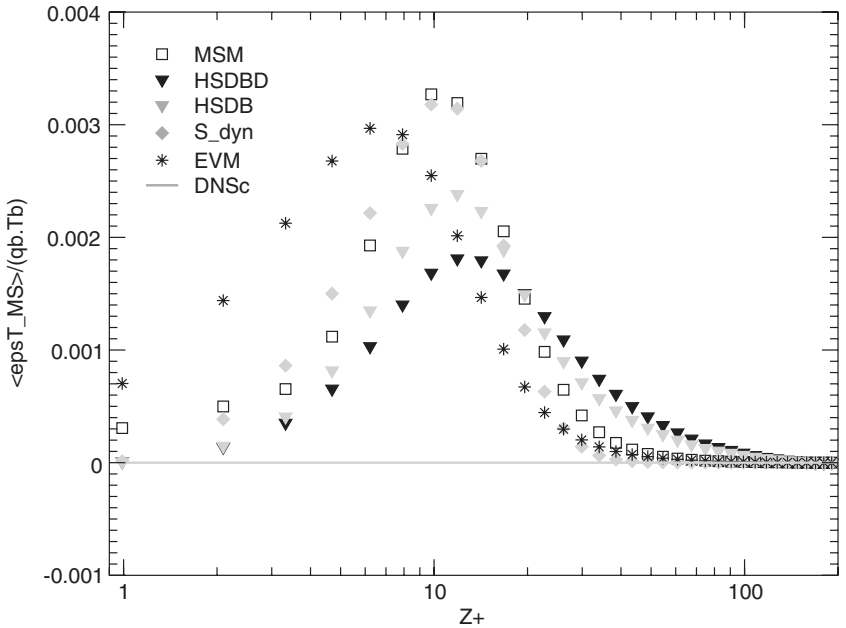

Figure 9. Mean SGS dissipation (fine grid): part related to the mean temperature gradient.

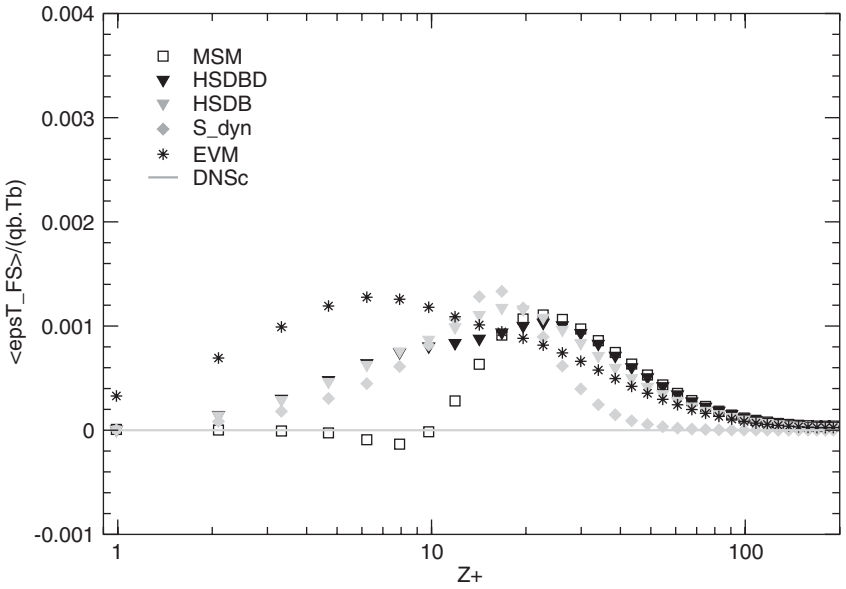

Figure 10. Mean SGS dissipation (fine grid): part related to the fluctuating field (right side).

associated with the fluctuating field happens to reach negative values. This feature of the model was also observed for the turbulent kinetic energy budget, in accordance with DNS data. Thus, it appears that the non-Fickian part of the model, even when coupled to a dynamic procedure, seems unable to recover the existence of the backscatter in average, although the instantaneous SGS dissipation can become negative. The EVM model has a different behaviour in the viscous layer compared to the others: the dissipation level is higher in this region which implies a lower wall temperature hence a diminution of friction temperature.

5.3. *Prandtl effect*

In order to study the Prandtl effect and compare empirical laws, it is necessary to normalize the statistical profiles of the temperature or heat flux by wall quantities such as the wall heat flux q_w defined by Equation (6) and the friction temperature T_w given by the following relation:

$$T_w = \frac{q_w}{u_w} \tag{26}$$

Figures 11–13 present the mean temperature profiles normalized by the wall temperature for three values of the Prandtl numbers ($Pr = \{0.10; 0.71; 2.00\}$) which are compared to empiric laws given by Kader *et al.* [30]. At the vicinity of the wall, the mean temperature profiles behave like Prz^+ while the mean temperature profiles behave like $(1/\kappa_\theta)\ln(z^+) + c_\theta(Pr)$ with $\kappa_\theta = 0.47$ and $c_\theta(Pr) = \{-4.64; 3.83; 14.08\}$ in the logarithmic region. For the three values of Prandtl numbers, the results are in good agreement when compared to both empiric laws and Kawamura's data except for the EVM model at $Pr = 2.00$: this model overestimates the mean temperature profile in the logarithmic region. It is important to notice the normalization

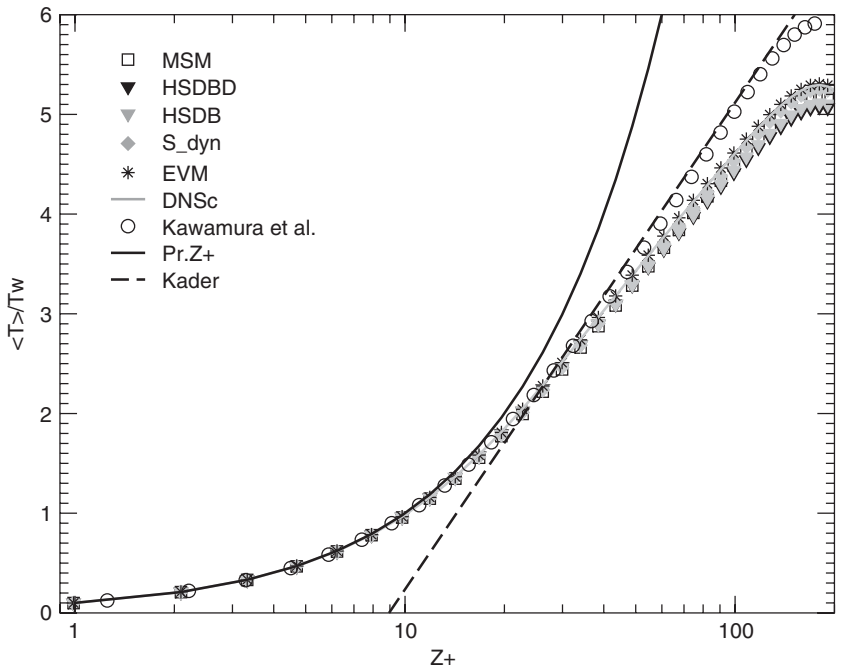

Figure 11. Mean temperature profiles normalized by the friction temperature: $Pr = 0.10$, fine grid.

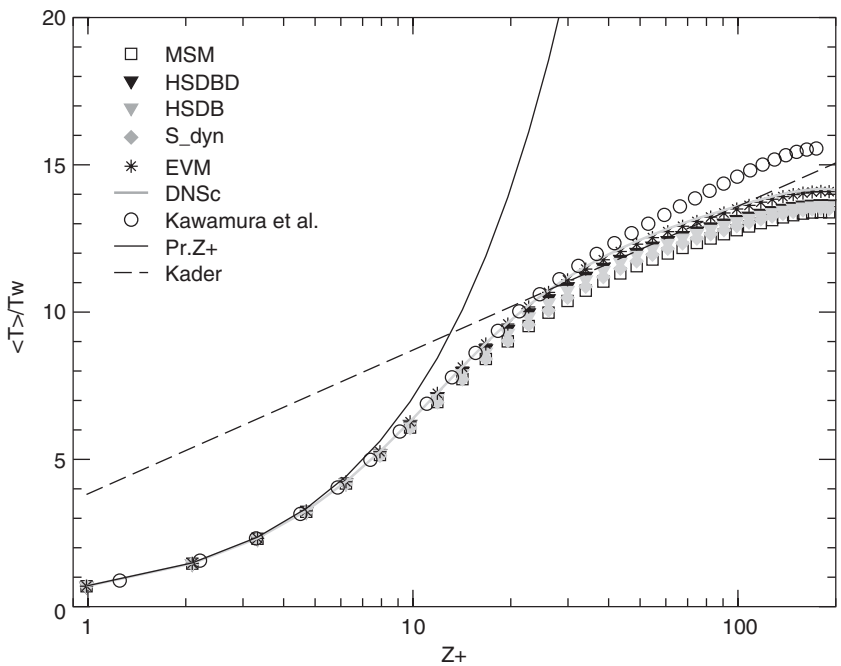

Figure 12. Mean temperature profiles normalized by the friction temperature: $Pr = 0.71$, fine grid.

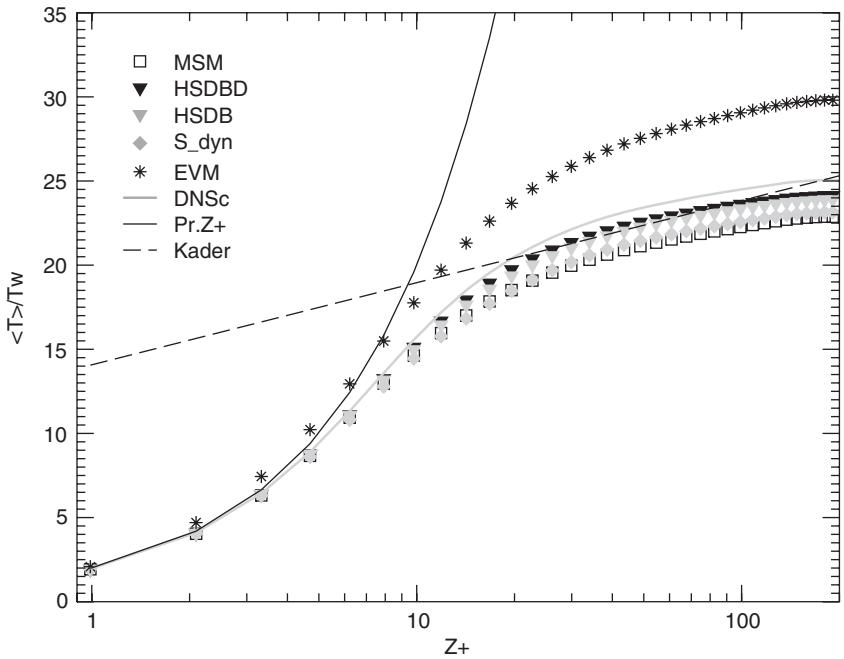

Figure 13. Mean temperature profiles normalized by the friction temperature: $Pr = 2.00$, fine grid.

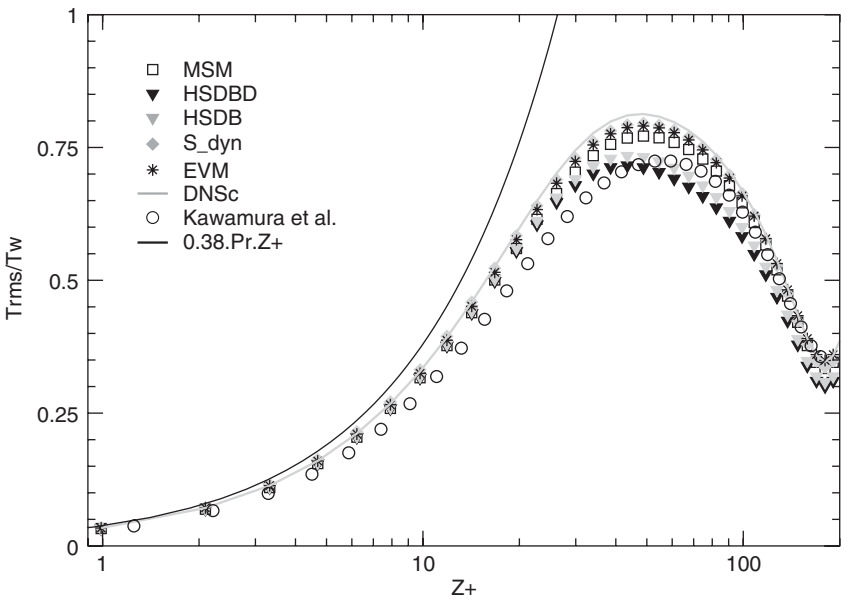

Figure 14. RMS temperature profiles normalized by the friction temperature: $Pr = 0.10$, fine grid.

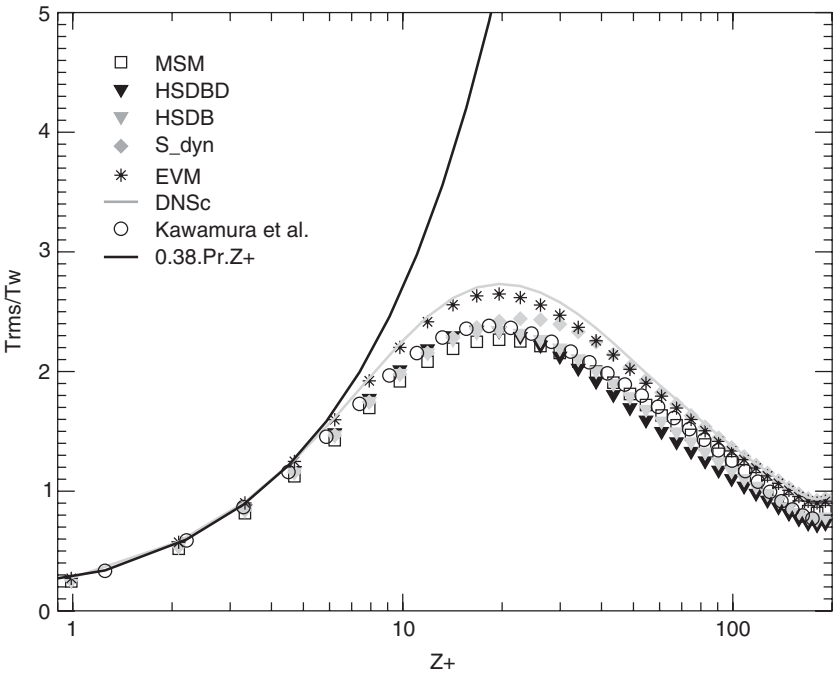

Figure 15. RMS temperature profiles normalized by the friction temperature: $Pr = 0.71$, fine grid.

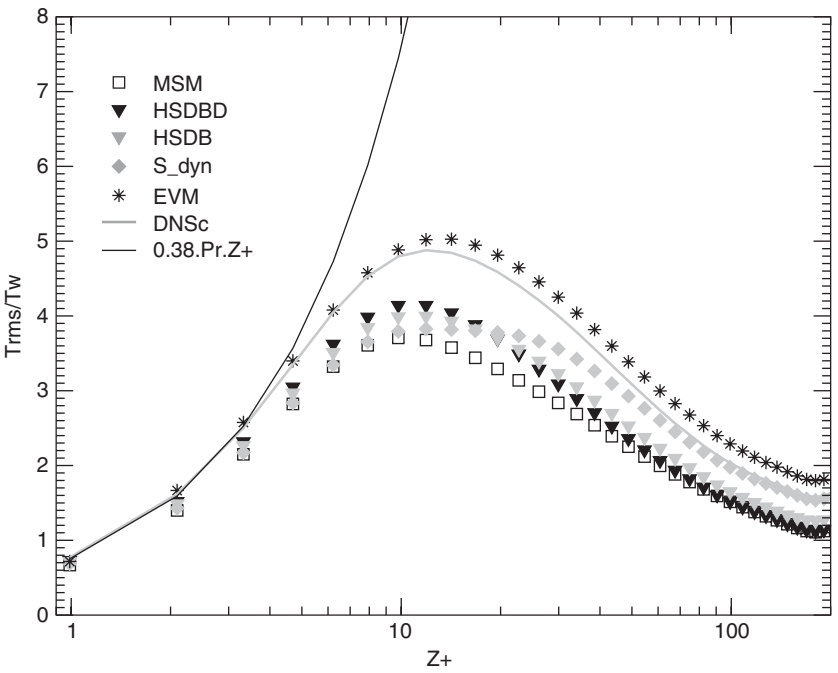

Figure 16. RMS temperature profiles normalized by the friction temperature: $Pr = 2.00$, fine grid.

effect. Indeed, Figures 1 and 12 describe the same mean temperature profiles: the first one is normalized by the bulk temperature, while the second one by the friction temperature. It is clear that the normalization points out discrepancies. This remark is still valid for the other kind of studied profiles (i.e. the RMS temperature, etc.). Figures 14–16 present the RMS temperature profiles for the same three Prandtl number values. Following Kawamura *et al.* [15], these quantities behave like $0.38Prz^+$ at the vicinity of the wall. The results are also in good agreement: the prediction of the peak (position and intensity) is well recovered except for the EVM model and the DNSc case.

6. INSTANTANEOUS FIELDS ANALYSIS

The following paragraphs present sections of instantaneous velocity and temperature fields. Although all the fields for each model are available, the figures presented below are issued from the fine mesh with the MSM model in order to analyse some physical phenomena such as sweeps and ejections, but also the coherent structures near the wall associated with the dynamical and thermal fields.

6.1. The thermal conduction zone highlighting

Figures 17 and 18 present a cross section of the instantaneous temperature and velocity fields and also the normal gradient of the temperature on the lower wall for two values of Prandtl number of this study (0.10 and 2.00). The cross sections at 0.71 Prandtl value are similar to the 2.00 Prandtl value case, so they are not presented here for brevity.

To make the comparison easier, the three sections are done at the same position ($x^+ = 0$) and at the same time ($\widetilde{t} = 1308$); consequently, the dynamical field represented by the velocity vectors on the three pictures are rigorously identical because the temperature field is simply carried by the turbulent velocity field. The three temperature fields are normalized by, respectively, the maximum value of the numerical domain at this time. We recall that the isoflux condition requires a zero wall temperature in blue on the figure, the maxima are located in the centre of the channel in pink. The height and width of the channel are expressed in wall units.

Scrutinizing Figure 17 which corresponds to the case $Pr = 0.10$, it is possible to distinguish three large zones. The first one near the wall in blue until $z^+ \simeq 10$–20 is the thermal conduction zone which is quite thick due to the low Prandtl number; in the latter the molecular effects rule over the scalar transport. The second green zone is identified as a buffer zone in which the molecular and convective effects are of the same order. The last zone in pink contains the logarithmic and central zones, there the convective effects are dominating.

The increasing of the Prandtl number value runs one into the diminution of the influence zone of the thermal conduction effects. In the second case (i.e. Figure 18: $Pr = 2.00$), the iso-values in green-blue are restricted to $z^+ = 20$.

The comparison of the wall temperature gradients of the three curves is very instructive. The peaks, related to the secondary flow impinging perpendicularly to the wall, are associated with the sweeps. The temperature field reacts like a passive scalar, it should play the role of tracer pointing out the presence of physical phenomena such as the sweep and the ejection.

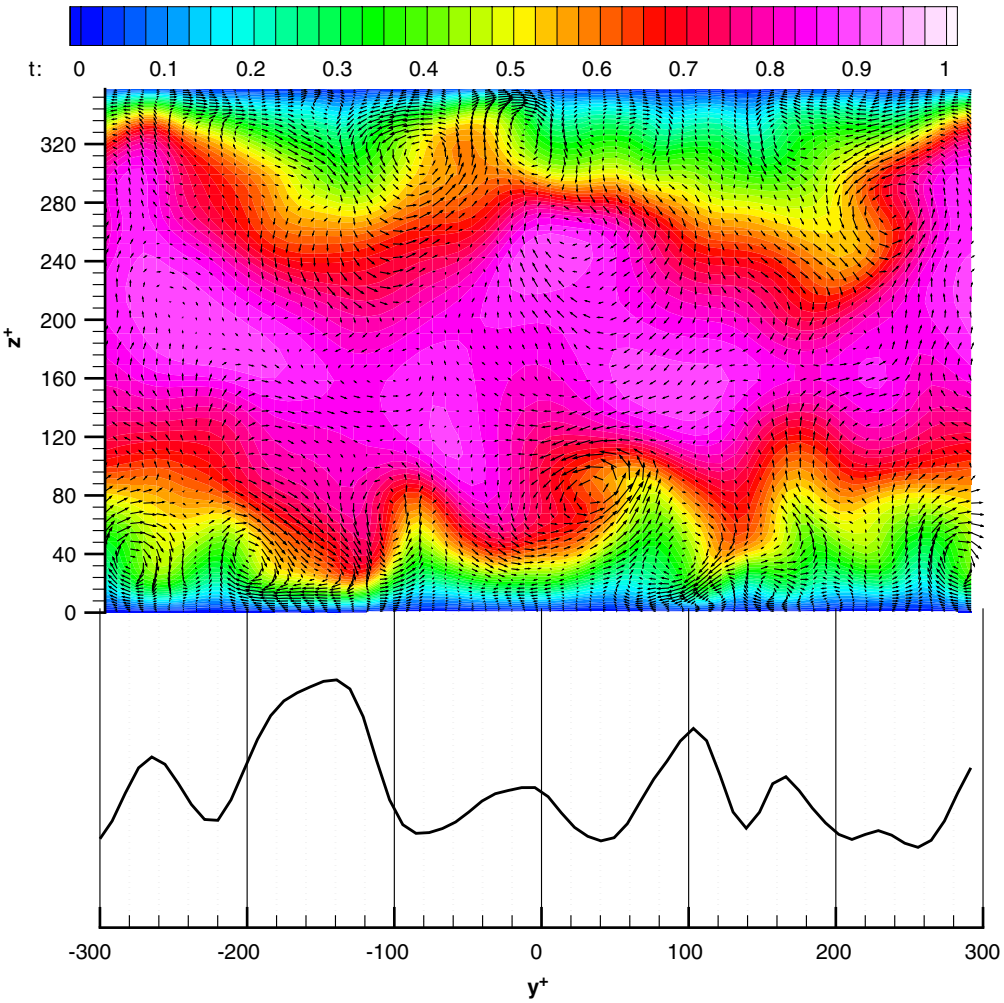

Figure 17. Top: cross section of velocity and temperature fields for $Pr = 0.10$. Bottom: normal temperature gradient on the lower wall normalized by its maximal value.

In the sections given by Figures 17 and 18, the neighbourhood of the point $x^+ = 0$, $y^+ = 100$ and $z^+ = 20$ seems to show the presence of a sweep.

6.2. *The coherent structures highlighting*

Different experiments and simulations showed the existence of structures in the neighbourhood of the wall, called 'streaks'. These structures are very thin, hot or cold streaks, which are stretched in the flow direction. In order to highlight the presence of these structures in our simulations, it is necessary to study the fluctuations of the velocity field in the main flow

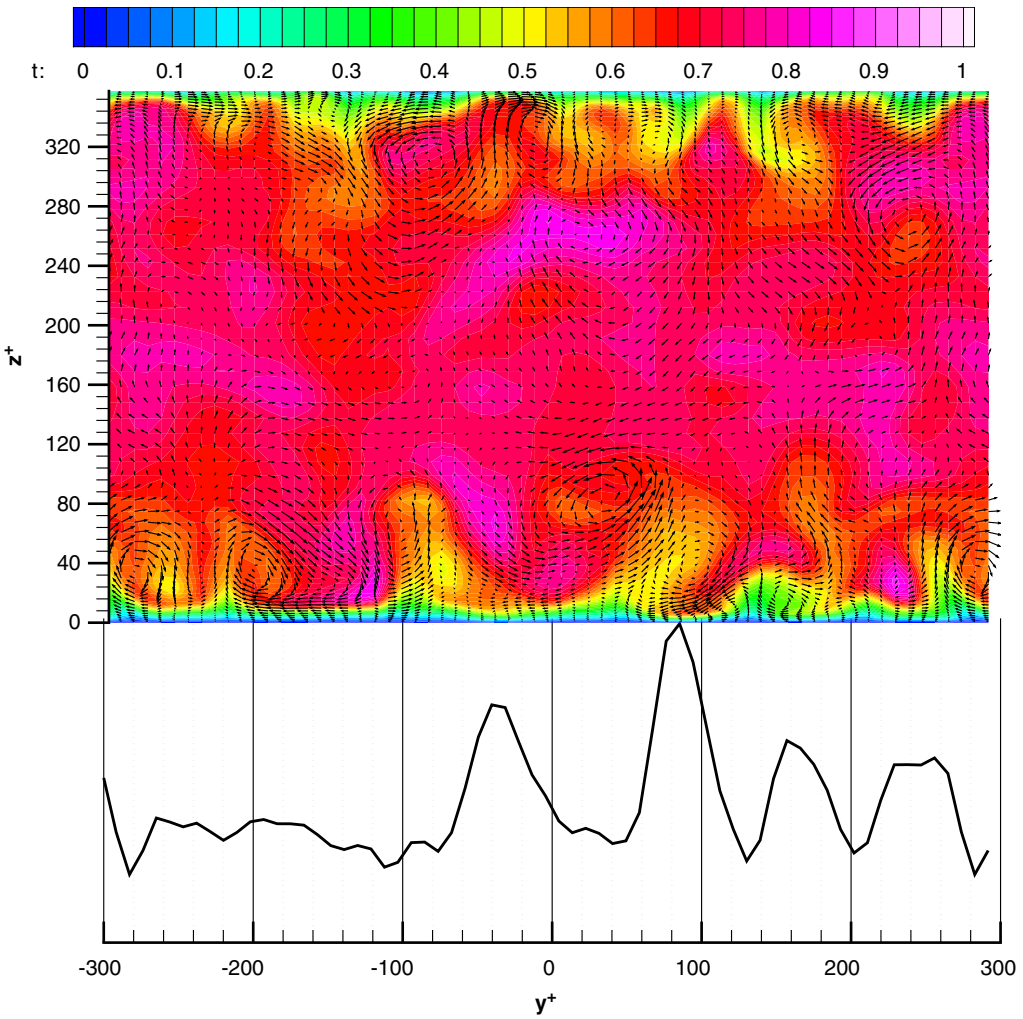

Figure 18. Top: cross section of velocity and temperature fields for $Pr = 2.00$. Bottom: normal temperature gradient on the lower wall normalized by its maximal value.

direction: we introduce a fluctuating field noted $\overline{U}'$ and defined by

$$\overline{U}'(x, y, z; t) = \overline{U}(x, y, z; t) - \langle \overline{U} \rangle_{XY}(z; t) \tag{27}$$

The iso-values $\overline{U}'$ normalized by the friction velocity are drawn in Figure 19. This case corresponds to the selective MSM for the fine mesh and $Re_\tau = 180$. The negative iso-values 'in blue' depict the slow flow zones, while the positive iso-values 'in red' correspond to the fast flow zones. The spacing and the length of these structures are adequate, of order 100 and 1000 wall units in average. About temperature field, some similar structures exist like those observed in the dynamical field. As a matter of fact, the temperature field is carried

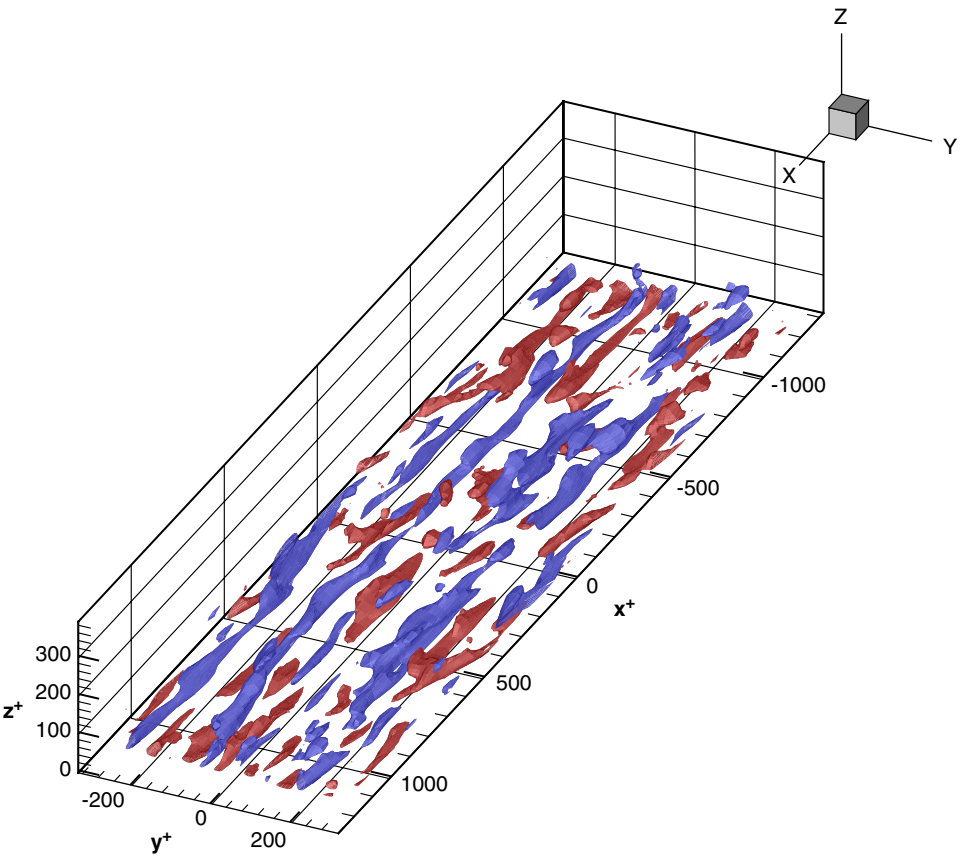

Figure 19. Velocity fluctuations iso-values normalized by the friction velocity: in blue, low-velocity zone ($\overline{U}'^{+} < -3.5$); in red, high-velocity zone ($\overline{U}'^{+} > +3.5$).

by the turbulent velocity field, then structures close to the streaks are expected. We need to study the temperature fluctuations and we introduce the fluctuating field: $\overline{\Theta}'$ defined by

$$\overline{\Theta}'(x, y, z; t) = \overline{\Theta}(x, y, z; t) - \langle \overline{\Theta} \rangle_{XY}(z; t) \tag{28}$$

In Figures 20 and 21 the iso-values of fluctuating temperature $\overline{\Theta}'$ normalized by the skin friction temperature for the fine mesh are plotted for the two values of the Prandtl number ($Pr = 0.10$ and 2.00). All the results are obtained with the MSM model. The negative iso-values 'in blue' correspond to the low-temperature region, while the zone 'in red' depicts the high-temperature regions. The shape of these structures depends on the Prandtl number, as we can see in Figures 20 and 21. This is in agreement with the results of Kim [31]: the correlation length for the temperature fluctuations in the cross direction is doubled for $Pr = 0.10$, compared to the case $Pr = 2.00$. Another phenomenon is noticeable in scrutinizing Figure 21. The low-velocity zones are associated with the low-temperature flow, because the

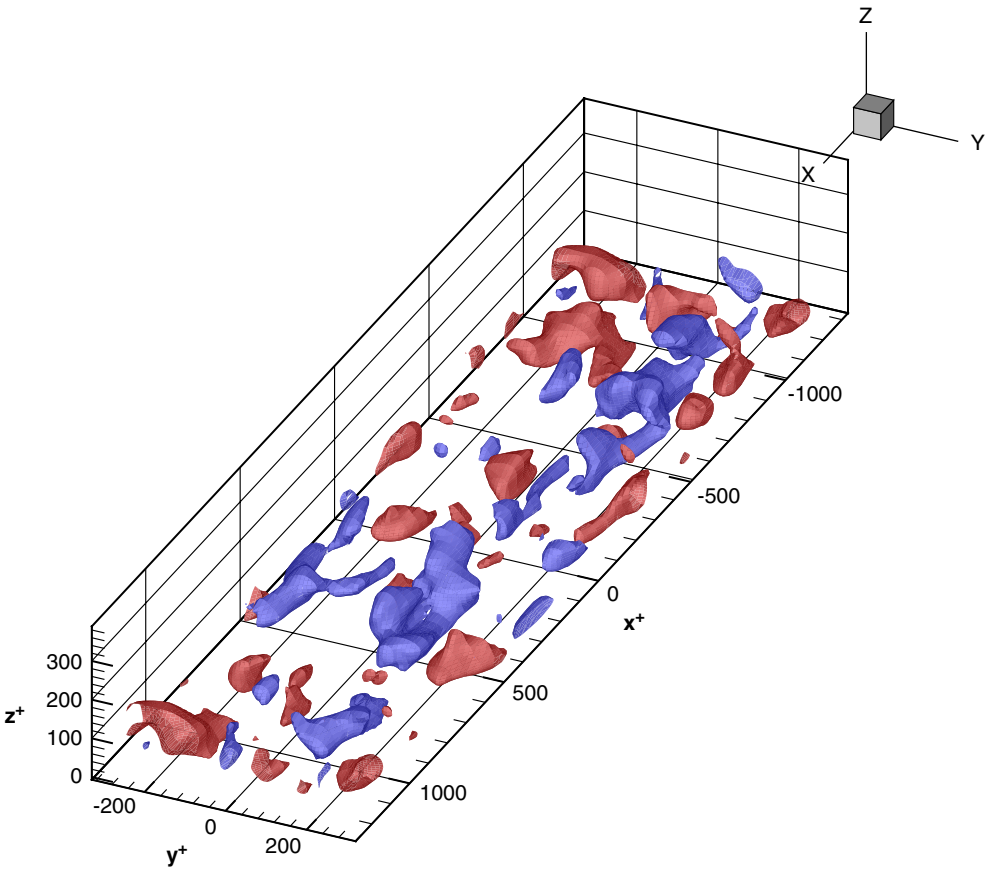

Figure 20. Temperature fluctuations iso-values normalized by the friction temperature for $Pr = 0.10$: in blue, low-temperature zone, ($\overline{\Theta}'^{+} < -1.0$); in red, high-temperature zone ($\overline{\Theta}'^{+} > +1.0$).

slow flow issued from the cold wall carries cold flow, while the fast flow from the core of the domain transports hot fluid.

7. CONCLUSIONS

Several SGS models for the passive scalar flux have been proposed and assessed on a heated plane channel configuration. These models incorporate a non-Fickian part, which was derived using the scale-similarity hypothesis or a second-order non-linear expansion.

The computed results are in good agreement with DNS data when looking at the mean temperature profile, but larger discrepancies are observed when looking at the second-order moments. The resolved turbulent Prandtl number is in good agreement with DNS data.

A careful analysis of the SGS dissipation shows that only the Fickian part of the HSDBD is able to account for backscatter in the buffer layer, but the global model is unable to capture this dynamical process. The MSM is found to be able to recover the backscatter when looking at the fluctuating field contribution, thanks to the use of the selection function.

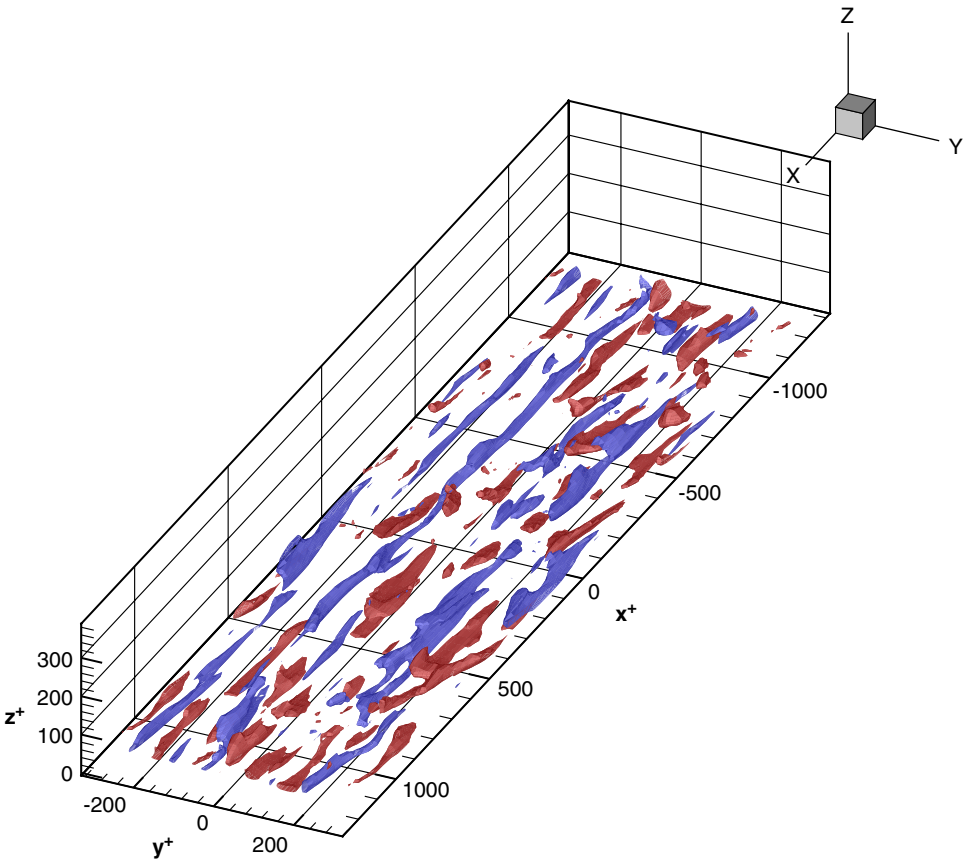

Figure 21. Temperature fluctuations iso-values normalized by the friction temperature for $Pr = 2.00$: in blue, low-temperature zone ($\overline{\Theta}^{\prime +} < -5.0$); in red, high-temperature zone ($\overline{\Theta}^{\prime +} > +5.0$).

In a consistent way, all the models presented here reproduce the following trend quite well: the conduction zone decreases while the Prandtl number increases and the maximum peak value increases and shifts towards the wall.

The instantaneous fields show that the sweeps induce wall heat transfer peaks whose intensity depends on the Prandtl number. These peaks are located in the vicinity of the secondary flow stagnation point.

The thermal coherent structure are strongly correlated with the dynamical coherent structure (streaks) all the more the Prandtl number values are close to or over unity.

REFERENCES

1. Deardoff JW. A numerical study of three-dimensional turbulent channel flow at large Reynolds numbers. *Journal of Fluid Mechanics* 1970; **41**:453–480.
2. Kim J, Moin P, Moser R. Turbulence statistics in fully developed channel flow at low Reynolds number. *Journal of Fluid Mechanics* 1987; **177**:133–166.

3. Mansour N, Moser R, Kim J. PCH11: fully developed turbulent channel flow simulations. *A Selection of Test Cases for the Validation of Large-Eddy Simulations of Turbulent Flows—AGARD Advisory Report 345*, 1998.
4. Moin P, Kim J. Numerical investigation of turbulent channel flow. *Journal of Fluid Mechanics* 1982; 341–377.
5. Sagaut P, Montreuil E, Labbé O, Cambon C. Analysis of the near-wall behavior of some self-adaptative subgrid-scale models in finite-differenced simulations of channel flow. *Journal for Numerical Methods in Fluids* 2002; **40**:1275–1302.
6. Kim J, Moin P. Transport of passive scalars in a turbulent channel flow. *Sixth Symposium on Turbulent Shear Flow*, 1987.
7. Teitel M, Antonia RA. Heat transfer in fully developed turbulent channel flow: comparison between experiment and direct numerical simulations. *International Journal of Heat and Mass Transfer* 1993; **36**:1701–1706.
8. Lyons SL. A direct simulation of fully developed turbulent channel flow with passive heat transfer. *Ph.D. Thesis*, University of Illinois, Urbana, Illinois, 1989.
9. Lyons SL, Hanratty TJ, McLaughlin JB. Large-scale computer simulation of fully developed turbulent channel flow with heat transfer. *International Journal for Numerical Methods in Fluids* 1991; **13**:999–1028.
10. Kasagi N, Kuroda A, Hirata M. Numerical investigation of near-wall heat transfer taking account the unsteady heat conduction in the solid wall. *Journal of Heat Transfer* 1989; **111**:385–392.
11. Kasagi N, Tomita Y, Kuroda A. Direct numerical simulation of passive scalar field in a turbulent channel flow. *Journal of Heat Transfer* 1992; **114**:598–606.
12. Calmet I, Magnaudet J. Large eddy simulation of high-Schmidt number mass transfer in a turbulent channel flow. *Physics of Fluids* 1997; 438–455.
13. Dong Y, Lu X, Zhuang L. Large eddy simulation of turbulent channel flow with mass transfer at high-Schmidt numbers. *International Journal of Heat and Mass Transfer* 2002; 1529–1539.
14. Kawamura H, Abe H, Matsuo Y. DNS of turbulent heat transfer in channel flow with respect to Reynolds and Prandtl number effects. *International Journal of Heat and Fluid Flow* 1999; **20**:196–207.
15. Kawamura H, Ohsaka K, Abe H, Yamamoto K. Direct numerical simulation of turbulent heat transfer in channel flow with low to medium-high Prandtl number fluid. *International Journal of Heat and Fluid Flow* 1998; **19**:482–491.
16. Wang L, Lu X. An investigation of turbulent oscillatory heat transfer in channel flows by large eddy simulation. *International Journal of Heat and Mass Transfer* 2003; 2161–2172.
17. Sagaut P. *Large-Eddy Simulation for Incompressible Flows—An Introduction* (2nd edn). Springer: Berlin, 2003.
18. Corrsin S. Limitations of gradient transport models in random walks and in turbulence. *Advances in Geophysics* 1974; **18A**:25–60.
19. Labbé O, Sagaut P, Montreuil E. Large-eddy simulation of heat transfer over a backward-facing step. *Journal of Numerical Heat Transfer*, *Part A*, 2002; **42**:73–90.
20. Welch JE, Harlow FH, Shannon JP, Daly BJ. The MAC method: a computing technique for solving viscous, incompressible, transient fluid flow problems involving free surfaces. *Technical Report*, Los Alamos Scientific Laboratory, 1966.
21. Sagaut P. Numerical simulations of separated flows with subgrid-scale models. *Aerospace Research* 1996; **1**: 51–63.
22. Salvetti MV, Banerjee S. A priori tests of a new dynamic subgrid-scale model for finite-difference large eddy simulations. *Physics of Fluids* 1995; **7**:2831–2847.
23. Lilly DK. A proposed modification of the Germano subgrid-scale closure method. *Physics of Fluids* 1992; **4**:633–635.
24. Yoshizawa A. Statistical modelling of passive scalar diffusion in turbulent shear flow. *Journal of Fluid Mechanics* 1988; **195**:544–555.
25. Schmidt H, Schumann U. Coherent structure of the convective boundary layer derived from large-eddy simulations. *Journal of Fluid Mechanics* 1989; **200**:511–562.
26. Lesieur M, Rogallo R. Large-eddy simulation of passive scalar diffusion in isotropic turbulence. *Physics of Fluids* 1988; **1**:718–722.
27. Métais O, Lesieur M. Spectral large-eddy simulation of isotropic and stably stratified turbulence. *Journal of Fluid Mechanics* 1992; **239**:157–194.
28. Herring JR, Shertzer D, Lesieur M, Newman GR, Chollet JP, Larchevêque M. A comparative assessment of spectral closures as applied to passive scalar diffusion. *Journal of Fluid Mechanics* 1982; **124**:411–437.
29. Härtel C, Kleiser L. Analysis and modelling of subgrid-scale motions in the near-wall turbulence. *Journal of Fluid Mechanics* 1998; **356**:327–352.
30. Kader BA. Temperature and concentration profiles in fully turbulent boundary layers. *International Journal of Heat and Mass Transfer* 1981; **24**:1541–1544.
31. Kim J. Investigation of heat transfer and momentum transport in turbulent flows via numerical simulations. *Transport Phenomena in Turbulent Flows*. Hemisphere: New York, NY, 1988; 715–729.

